CHAPTER V

WAVE PACKET INTERFEROMETRY AND ELECTRONIC ENERGY TRANSFER

Introduction[1]

Advances in controlling[2,3] or monitoring[4] the inter-pulse delays within sequences of femtosecond laser pulses with sub-optical-period accuracy have triggered the development of new electronic interference spectroscopies in which the signal is quadralinear in external fields bearing precisely specified optical phase relationships to one another.[5,6,7] The power of these techniques for elucidating chemical dynamics lies in generating coherent signals that are directly proportional to the overlap between multi-pulse target and reference nuclear wave packets (in a pure-state description) or to a multi-pulse density matrix increment (in a mixed-state treatment). This feature stands in contrast to more standard homodyne-detected four-wave mixing spectroscopies, which measure quantities proportional to the absolute-value-squared of the corresponding overlap or density matrix increment and do not require phase-controlled pulse sequences. It also differs from ultrafast pump-probe[8] and time-resolved fluorescence[9] spectroscopies, which are linear in a density matrix increment but *bilinear* in each of two external pulses (pump and probe or gate) and which to first approximation monitor time-dependent nuclear probability densities[10] rather than overlaps between distinct amplitudes. The latter two examples additionally require a compromise between time-resolution (pulse duration) and frequency resolution (spectral selectivity) in at least one of the pulses, whereas amplitude-sensitive interference spectroscopy approaches

its ideal realization with pulses short enough to freeze nuclear motion on the fastest timescales.

The experimental study of amplitude-sensitive nonlinear electronic spectroscopy was initiated by Wiersma and co-workers with their measurement of phase-locked heterodyne-detected stimulated photon echoes (pl-HSPE) from dye molecules in solution.[5,11] The current state of progress in the field is exemplified by Jonas and co-workers' recent two-dimensional Fourier-transform study of electronic transitions in another solvated laser dye.[7] In addition to incorporating a number of technical improvements, those experiments[7] may reveal additional information about nonresonant effects because they employ an external reference field that does not pass through the sample. There have been parallel advances in heterodyne-detected multi-dimensional vibrational spectroscopy of both solvated chromophores[12] and neat liquids.[13]

Theory has guided all of these developments. The phase-locked heterodyned photon echo (and the closely related three-pulse phase-locked pump-probe absorption) was suggested by Cho et al.[14] Tanimura and Mukamel[15] analyzed the prospects for multi-dimensional vibrational spectroscopy prior to its successful implementation. Theoretical studies by Metiu and Engel[16] prefigured the original experiments on linear interference spectroscopy with phase-locked pulses.[2,3]

Despite the experimental progress and the contributions from theory in elucidating the physical content of ultrafast electronic interference measurements, much work remains to be done toward interpreting these signals in terms of the underlying molecular processes. In this context, it is desirable to seek detailed pictures of many-body condensed-phase dynamics similar to those that have emerged from relatively simpler pump-probe experiments[17] and time-resolved coherent anti-Stokes Raman scattering (tr-CARS) signals from chromophores in low-temperature matrices.[18] The most illuminating interpretations in

each case have been wavepacket descriptions akin to those originally devised for linear absorption[19] and resonance Raman[20] data.[21,22,10,23,24]

In previous research that helped develop wavepacket pictures for multi-dimensional interference experiments, we analyzed the ability of nonlinear wavepacket interferometry measurements equivalent to the pl-HSPE to prepare and measure superpositions between differently-handed states in the double-well potential of a chiral molecule.[25] More recently, we have shown that nonlinear wavepacket interferometry has the capacity to reveal the complex-valued overlaps between a given short-pulse-generated target wavepacket on an excited potential energy surface of a polyatomic molecule and an exhaustive collection of variable reference wave packets.[26,27] Among other uses, this form of wavepacket interferometry could serve as a diagnostic tool for quantum control[28] and molecule-based quantum information processing.[29]

Here we make a detailed study of multi-dimensional time-domain electronic interference spectra for a model complex supporting electronic energy transfer, and interpret their form in terms of the amplitude dynamics of the nuclear wave packets on and between donor-excited and acceptor-excited electronic potential energy surfaces. The ultrafast dynamics of electronic energy transfer in photosynthetic light-harvesting complexes,[30] J-aggregates,[31] and various model complexes[32,33,34,35] has been the focus of intensive investigation. This prototypical process in chemical dynamics was described by Förster in an insightful heuristic treatment.[36] A more rigorous treatment, which generalizes the original description by incorporating electronic coherence and inter- as well as intramolecular motion was later put forward by Rackovsky and Silbey[37] and Soules and Duke.[38,39] While the focus in prior studies has mostly been on donor- and acceptor-state population dynamics or nuclear probability densities (proportional to the square and higher even powers of the transfer matrix element J), we show here that wavepacket interferometry

measurements are sensitive to the nuclear probability amplitude (linear in J) for electronic energy transfer.

Our model energy-transfer complex is a simple one amenable to detailed analysis. It comprises a pair of interacting two-level chromophores whose electronic transition dipole moments are fixed in space. Donor and acceptor chromophores each support a single intramolecular vibration. We touch on the issue of inhomogeneous broadening of the electronic transition frequencies, but defer until later the incorporation of important features such as multiple intra-and intermolecular vibrational modes, orientational disorder, electronic dephasing, and thermal congestion.[40] By illustration with this model complex, we show that nonlinear wavepacket interferometry, together with the tools of optical phase control and polarization spectroscopy, is directly sensitive at the amplitude level to the dynamics of inter-nuclear motion accompanying and giving rise to energy-transfer surface-crossing transitions. It has the capacity to monitor the basic process of electronic-nuclear state entanglement that underlies energy transfer, and ameliorates a long-perceived shortcoming of conventional measurements on two-electronic-state systems.[41]

Basic Theory

We consider a dimer complex whose Hamiltonian,

$$H = |0\rangle H_0 \langle 0| + |1\rangle H_1 \langle 1| + |1\rangle H_1 \langle 1| + |2\rangle H_0 \langle 2| + J\{|1\rangle\langle 1| + |1\rangle\langle 1|\} \tag{5.1}$$

comprises four electronic levels: $|0\rangle = |g_a g_b\rangle$ with both molecules unexcited, $|1\rangle = |e_a g_b\rangle$ with the "donor" excited, $|1\rangle = |g_a e_b\rangle$ with the "acceptor" excited, and $|2\rangle = |e_a e_b\rangle$ with both molecules excited. The corresponding nuclear Hamiltonians,

$$H_j = \frac{p_a^2}{2m} + \frac{p_b^2}{2m} + v_j(q_a, q_b)\,, \tag{5.2}$$

with potential energy surfaces,

$$v_0 = \frac{m \quad ^2}{2}(q_a^2 + q_b^2), \tag{5.3}$$

$$v_1 = \quad _1 + \frac{m \quad ^2}{2}((q_a \quad d)^2 + q_b^2), \tag{5.4}$$

$$v_1 = \quad _1 + \frac{m \quad ^2}{2}(q_a^2 + (q_b \quad d)^2), \tag{5.5}$$

$$v_2 = \quad _2 + \frac{m \quad ^2}{2}((q_a \quad d)^2 + (q_b \quad d)^2), \tag{5.6}$$

govern the motion of one intramolecular vibration in each chromophore. The equilibrium position of a vibrational mode is displaced by a distance d when the host molecule is electronically excited. The site energy of the two-exciton state is typically $\quad _2 \quad _1 + \quad _1$.[42,43]

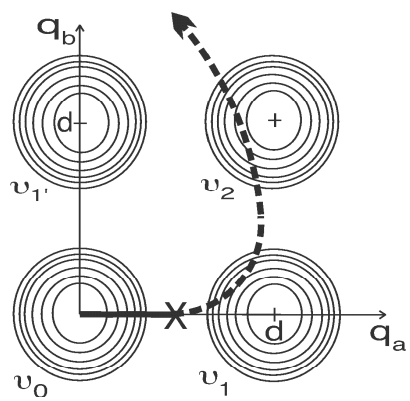

Fig. 5.1 Schematic contour plots of potential energy surfaces for electronic ground state, donor excited state, acceptor excited state, and two-exciton state. The minimum of energy in each potential is at the corresponding site energy, as in Eqs. (5.3) – (5.6). A sketch of the spatial path for a possible contribution to the target wave packet is also shown.

Figure 5.1 shows a contour plot of the four site potential energy surfaces.[44] A state change from 1 to 1 — energy transfer from donor to acceptor — is expected to proceed efficiently at positions where $v_1 = v_1$. This intersection occurs along a diagonal line $q_b = q_a \quad (\quad _1 \quad _1)/m \quad ^2 d$ whose location depends on the site-energy difference between donor and acceptor moieties.[45] As energy transfer ensues, an entangled state develops

through the process $|1\rangle|\ \ _1\rangle\ \ |1\rangle|\ \ _1\rangle+|1\ \rangle|\ \ _1\ \rangle$. While the transferred population, $\langle\ \ _1|\ \ _1\rangle$, is often measured, and some information about the time-evolution of the probability density, $|\ \ _1(q_a,q_b)|^2$, has already been obtained from ultrafast experiments, there does not yet appear to have been a direct determination of the entangled state itself, nor in particular, of the transferred *amplitude* $|\ \ _1\rangle$.

We shall see that wavepacket interferometry with optically phase-locked ultrashort-pulse sequences can reveal the complex-valued overlap of a "target" wavepacket describing the energy-transfer amplitude with a collection of reference wave packets of specified structure. The ultrashort pulses that generate the target and reference wave packets will be part of a phase-controlled sequence, so we treat the evolution of the system under the time-dependent Hamiltonian $H(t)=H+V_I(t)$, where

$$V_I(t)=-\hat{\ }\ \mathbf{E}_I(t);\quad I=A,B,C,D \tag{5.7}$$

describes the interaction with one of four pulses,

$$\mathbf{E}_I(t)=\boldsymbol{e}_I A_I(t\quad t_I)\cos(\ \ _I(t\quad t_I)+\ \ _I), \tag{5.8}$$

each of which has a well defined polarization, envelope function, arrival time, carrier frequency, and phase. The intervals between pulses are referred to as $t_p=t_B\quad t_A$, $t_w=t_C\quad t_B$, and, $t_d=t_D\quad t_C$.[46] The electronic dipole moment operator,

$$\hat{\ }=\ \ _a\left(|1\rangle\langle 0|+|2\rangle\langle 1\ |\right)+\ \ _b\left(|1\ \rangle\langle 0|+|2\rangle\langle 1|\right)+\text{H.c.}\ , \tag{5.9}$$

allows transitions in which the exciton number changes by one. For our purposes, it is important that the molecular dipoles be nonparallel, so that pulses of different polarization can selectively address either the donor or the acceptor.

The experimental observable will be the portion of the population of a specific excited electronic state that is *quadrilinear* in the field amplitudes (i.e. proportional to

$A_A A_B A_C A_D$) immediately following the four-pulse sequence.[47] To calculate that population, it is sufficient to have the perturbative wave function,

$$\left| \quad (t)\right\rangle = [t \quad t_D](1+D)[t_d](1+C)[t_w](1+B)[t_p](1+A)[t_A \quad t_0]\left| \quad (t_0)\right\rangle, \tag{5.10}$$

in which the molecular evolution operators[48] are written as $[t] = \exp(\ iHt)$ and pulse overlap has been neglected.[49] The operators $I = A, B, C,$ and D are pulse propagators,[50]

$$I = \ i \quad d\ [\quad + t_I]V_I(\ )[\ \ - t_I], \tag{5.11}$$

whose forms are simplified by neglecting energy transfer during the pulses and adopting the rotating wave approximation.[51]

In calculating the amplitude in each of the excited states, we take note of the fact that an odd number of laser-molecule interactions (one or three) are required to reach either of the one-exciton states, while an even number (two or four) are needed to reach the two-exciton state. For the nuclear wave function in the acceptor-excited state, we find

$$\begin{aligned}\left| \quad {}_1(t)\right\rangle = \langle 1 \,|[t - t_D]\Big\{ & D[t_d + t_w + t_p] + [t_d]C[t_w + t_p] \\ & + [t_d + t_w]B[t_p] + [t_d + t_w + t_p]A \\ & + D[t_d]C[t_w]B[t_p] + D[t_d]C[t_w + t_p]A + \\ & D[t_d + t_w]B[t_p]A + [t_d]C[t_w]B[t_p]A\Big\}|0\rangle|n_0\rangle.\end{aligned} \tag{5.12}$$

Similar expressions can readily be found for the nuclear probability amplitude in the other electronic states.[52]

Since we are interested in the amplitude for 1 1 electronic energy transfer of first order in J, we need to examine the contributions to $\left| \quad {}_1\right\rangle$ that are first and zeroth order in J. The former are possible target wave packets while the latter are available as reference states. Keeping contributions to the free evolution operator that are zeroth and first order in J,[53]

$$[t] = [t]_0 + [t]_1 , \tag{5.13}$$

we can re-write Eq. (5.12) as

$$\begin{aligned} |\ _1(t)\rangle = &|A_1\rangle + |B_1\rangle + |C_1\rangle + |D_1\rangle \\ &+ |(JA)_1\rangle + |(JB)_1\rangle + |(JC)_1\rangle + |(JD)_1\rangle \\ &+ |(DCB)_1\rangle + |(DCA)_1\rangle + |(DBA)_1\rangle + |(CBA)_1\rangle \\ &+ |(JDCB)_1\rangle + |(DCJB)_1\rangle + |(JDCA)_1\rangle + |(DCJA)_1\rangle \\ &+ |(JDBA)_1\rangle + |(DBJA)_1\rangle + |(JCBA)_1\rangle + |(CBJA)_1\rangle , \end{aligned} \tag{5.14}$$

which uses the short-hand notation

$$|(DCJB)_1\rangle = \langle 1\ |[t - t_D]_0 D[t_d]_0 C[t_w]_1 B[t_p]_0 |0\rangle |n_0\rangle , \tag{5.15}$$

and so forth.

In order to calculate the interference population P_1, we must identify the quadralinear contributions[54] to $\langle\ _1|\ _1\rangle$: a sum of four terms that are zeroth order in J (e.g., $2\mathrm{Re}\langle (DCB)_1 |(A)_1\rangle$) and twelve terms that are first order in J (e.g., $2\mathrm{Re}\langle (DCB)_1 |(JA)_1\rangle$).[55] But the situation can simplify considerably when we take account of laser polarization, as each of the amplitudes in Eq. (5.14) depends on the relative orientation of the field polarizations and molecular dipole moment operators.[56]

Case Study

We consider a simple example illustrating some basic features of interference measurements of energy transfer: the dimer is assigned a well defined internal and lab-frame geometry—as in a cryogenic matrix, macromolecular crystal, or layered

structure[57]—with $_a = \boldsymbol{i}$ and $_b = \boldsymbol{j}$ along the *space-fixed* x and y axes, respectively. Then x-polarized pulses can drive the transitions

$$1' \longleftrightarrow 2$$

$$0 \longleftrightarrow 1 \tag{5.16}$$

while y-polarized pulses drive the transitions

$$\begin{array}{cc} 1' & 2 \\ \updownarrow & \updownarrow \\ 0 & 1 \end{array} \tag{5.17}$$

Target amplitude on the acceptor state of first order in J can result from energy transfer following excitation of the donor state by an x-polarized laser pulse:

$$\begin{array}{ccc} 1' & & \\ & \nwarrow^{J} & \\ 0 & \longrightarrow & 1 \end{array} \tag{5.18}$$

Preparation of a reference wavepacket (zeroth order in J) that can interfere with this 1 target requires one (or three) y-polarized pulses and two (or no) x-polarized pulses. The former case (with a total of three x-polarized pulses and one y-polarized pulse) is suitable for our purposes, as it affords a wide variety of reference packets with both modes of vibration set in motion. This feature is useful in generating overlap with a target state whose a-mode is set moving after short-pulse excitation of the donor and whose b-mode motion is initiated by energy transfer.

We consider four different polarization combinations: $A_yB_xC_xD_x$, $A_xB_yC_xD_x$, $A_xB_xC_yD_x$, and $A_xB_xC_xD_y$. Under the first of these, the acceptor-state amplitude reduces to

$$|\ _{1'}(t)\rangle = \left|(A_y)_{1'}\right\rangle + \left|(JB_x)_{1'}\right\rangle + \left|(JC_x)_{1'}\right\rangle + \left|(JD_x)_{1'}\right\rangle \tag{5.19}$$

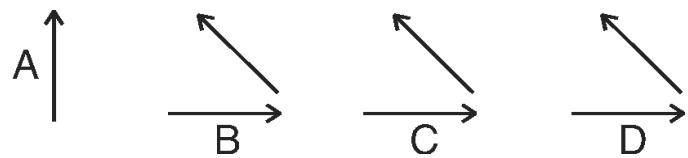

$$+ \left|\left(D_x C_x A_y\right)_{1'}\right\rangle + \left|\left(D_x B_x A_y\right)_{1'}\right\rangle + \left|\left(C_x B_x A_y\right)_{1'}\right\rangle$$

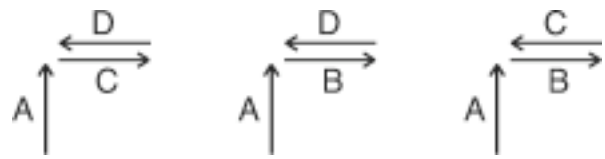

$$+ \left|\left(JD_x C_x B_x\right)_{1'}\right\rangle + \left|\left(D_x C_x JB_x\right)_{1'}\right\rangle$$

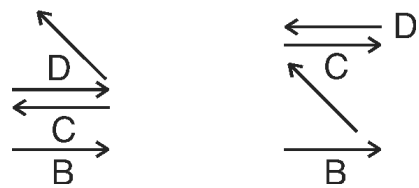

The resulting quadralinear contribution to $\langle\ _1(t)|\ _1(t)\rangle$ specifies the interference contribution to the acceptor-excited state population:

$$P_1\,(A_y B_x C_x D_x) \tag{5.20}$$

$$= 2\,\mathrm{Re}\Big\{\left\langle\left(A_y\right)_1 \middle|\left(JD_x C_x B_x\right)_1\right\rangle + \left\langle\left(A_y\right)_1 \middle|\left(D_x C_x JB_x\right)_1\right\rangle + \left\langle\left(D_x C_x A_y\right)_1 \middle|\left(JB_x\right)_1\right\rangle$$

$$+ \left\langle\left(D_x B_x A_y\right)_1 \middle|\left(JC_x\right)_1\right\rangle + \left\langle\left(C_x B_x A_y\right)_1 \middle|\left(JD_x\right)_1\right\rangle\Big\}.$$

As expected, this signal contains no terms of zeroth order in J.

It is useful to consider specific values of the relative optical phases of the pulses. Under a generalization of the phase-locking scheme developed by Scherer and co-workers for linear wavepacket interferometry with phase-locked pulse pairs,[2,3] it should be possible to make sequences of the form (5.8) comprising *pairs* of pulse-pairs AB and CD with intra-pair optical phase shifts

$$= \quad + \ _p t_p + \ _p \quad \text{and} \quad \ _D = \ _C + \ _d t_d + \ _d\,, \tag{5.21}$$

respectively. The phase shift $_p$($_d$) is termed the locking angle of the *AB (CD)* pulse-pair at the locking frequency $_p$($_d$). The *inter*pulse-pair phase shifts need not be controlled, so the angles $_D$ $_B$, $_D$ $_A$, $_C$ $_B$, and $_C$ $_A$ are assumed to sample a full range of values from 0 to 2 over many laser shots.[58]

The expressions (5.7), (5.8), and (5.11) show that parts of a pulse propagator *I* which induce upward transitions (proportional to $|1\rangle\langle 0|$, $|1\rangle\langle 0|$, $|2\rangle\langle 1|$, and $|2\rangle\langle 1|$) contain a phase factor exp(i $_I$). Parts of *I* that induce downward transitions (proportional to $|0\rangle\langle 1|$, $|0\rangle\langle 1|$, $|1\rangle\langle 2|$, and $|1\rangle\langle 2|$) contain a phase factor exp(i $_I$). As a result, we see that the last two terms in (5.20) are not phase controlled and hence average to zero over many repetitions. Using the optical phases (5.21), we find that

$$P_1(\ _p,\ _d) \tag{5.22}$$

$$= 2\,\mathrm{Re}\Big\{\exp(\ i\ _p\ \ i\ _d)\Big(\big\langle (A_y)_1 \big|(JD_xC_xB_x)_1\big\rangle^{(0)} + \big\langle (D_xC_xA_y)_1 \big|(JB_x)_1\big\rangle^{(0)}\Big)$$

$$+\ \exp(\ i\ _p + i\ _d)\big\langle (A_y)_1 \big|(D_xC_xJB_x)_1\big\rangle^{(0)}\Big\},$$

in which the superscript (0) designates the overlap with both pulse-pairs in-phase (i.e. $_p = \ _d = 0$). While three distinct overlaps can contribute to the interference signal (5.22) for a specific choice of the phase-locking angles, it is possible to combine signals with different phase-shifts in order to isolate the combinations

$$\big\langle (A_y)_1 \big|(JD_xC_xB_x)_1\big\rangle^{(0)} + \big\langle (D_xC_xA_y)_1 \big|(JB_x)_1\big\rangle^{(0)} \tag{5.23}$$

$$= \tfrac{1}{4}\big\{P_1(0,0) + P_1(\tfrac{\ }{2},\ \ \tfrac{\ }{2}) + iP_1(\tfrac{\ }{2},0) + iP_1(0,\tfrac{\ }{2})\big\}$$

and

$$\left\langle \left(A_y\right)_1 \middle| \left(D_x C_x J B_x\right)_1 \right\rangle^{(0)} = \tfrac{1}{4}\left\{ P_1(0,0) \quad P_1(\tfrac{}{2}, \ \tfrac{}{2}) + iP_1(\tfrac{}{2},0) \quad iP_1(0,\tfrac{}{2}) \right\}. \tag{5.24}$$

Combining signals with different values of $_p$ and $_d$ by the prescriptions (5.23) and (5.24) is an example of "phase cycling" in optical spectroscopy.[59,60] Equation (5.24) illustrates a key prediction of our analysis, that nonlinear wavepacket interferometry with pairs of pulse-pairs is capable of isolating the full complex overlap[61] $\langle \ _1 | \ _1 \rangle = \left\langle \left(A_y\right)_1 \middle| \left(D_x C_x J B_x\right)_1 \right\rangle^{(0)}$ between a given energy-transfer target

$$| \ _1 \rangle = \exp(i \ _B) \langle 1 \, | [t_w]_1 B_x | 0 \rangle | n_0 \rangle , \tag{5.25}$$

generated by first-order energy transfer during t_w, and the members of a collection of variable reference wave packets

$$| \ _1 \rangle = \left\{ \exp(i \ _B) \langle 1 \, | C_x^\dagger[-t_d]_0 D_x^\dagger[t_d + t_w + t_p]_0 A_y[-t_p]_0 | 0 \rangle | n_0 \rangle \right\} \Big|_{\ _p = \ _d = 0} \tag{5.26}$$

The *C* and *D* pulse propagators are reassigned to the reference wavepacket in Eq. (5.26) in order to highlight the correspondence between (5.25) and (5.18); some phase factors have been introduced in both bra and ket to render the target wavepacket independent of t_p and $_p$. Notice that the reference state evolves *backwards* in the two-exciton state during t_d.

The remaining polarization combinations of immediate interest are considered in Appendix A. A complete scan of inter-pulse delays would also include the two interleaved pulse sequences *ACBD* and *ACDB*; these alternative orderings provide some interesting overlaps, but we do not pause to analyze them here.

Energy-transfer Wave Packet Dynamics

A quasi-classical analysis of phase-space trajectories can indicate when the overlap $\langle \ _1 | \ _1 \rangle$, experimentally isolable according to Eq. (5.24), should be nonvanishing. A

schematic trajectory for the dominant portions of the target wavepacket $|\ _1\rangle$ is shown in Fig. 5.2. We specialize to energy-transfer waiting times equal to half a vibrational period, $t_w = \ _{\mathrm{vib}}/2 = \ /\ $, in order to allow time for only one crossing of the intersection between the $v_1(q_a,q_b)$ and $v_1\ (q_a,q_b)$ surfaces, and show the average values of *a*-mode and *b*-mode position and momentum that should result when the energy-transfer transition from 1 to 1 occurs after t_w in state 1. After the surface-crossing transition, the *a*-mode trajectory sweeps out an angle $(1\ \ )$ about $(\ q_a,\dot{q}_a) = (0,0)$; this is *twice* the angular displacement about the same origin that would have occurred if energy transfer had not taken place.[62,63] Meanwhile, the *b*-mode undergoes an angular displacement by $(1\ \ )$ about $(\ q_b,\dot{q}_b) = (\ d,0)$ after energy transfer.

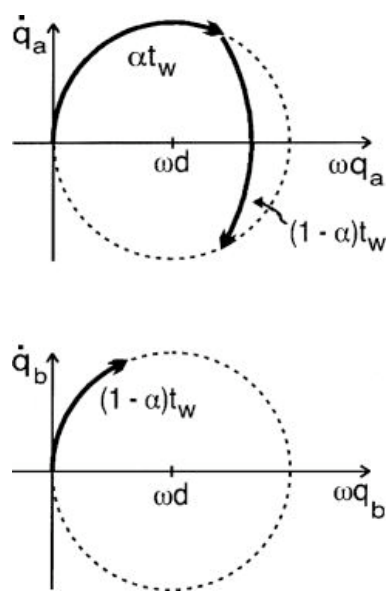

Fig. 5.2 Phase-space trajectories for the *a*-mode and *b*-mode of a target wave packet prepared by an *x*-polarized *B*-pulse. 1' ← 1 energy transfer is shown occurring after t_w of motion in the donor-excited state.

A schematic diagram of the phase-space motion for the reference wavepacket $\left| \quad {}_1 \right\rangle$ is shown in Fig. 5.3. In order for the target and reference wave packets to overlap significantly, their phase-space coordinates must nearly coincide. Comparison with Fig. 5.2 indicates that sizable overlap should occur for

$$t_p = \quad m+1 \quad \frac{}{2} \quad {}_{vib} \tag{5.27}$$

and

$$t_d = \quad n+\frac{}{2} \quad {}_{vib}\,, \tag{5.28}$$

where m and n are non-negative integers.

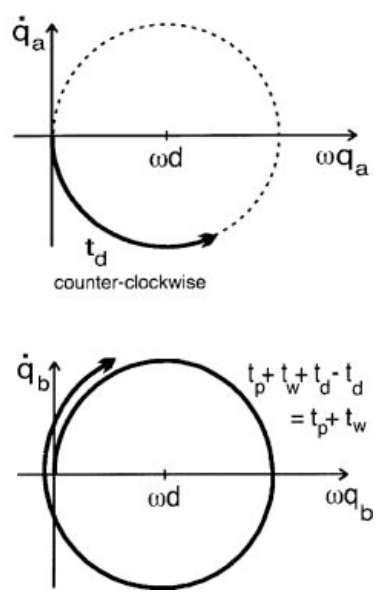

Fig. 5.3 Phase-space trajectories for the a-mode and b-mode of a reference wave packet prepared by A_y, C_x , and D_x pulses. The last two pulses operate in reverse order, with an interval t_d of backward evolution between them.

It is possible to obtain a closed-form expression for the isolable overlap (5.24) in the short-pulse limit (pulse duration much less than the inverse absorption bandwidth or inverse Franck-Condon energy). Analytic forms are given in Appendix E for the target

(E.5) and reference (E.7) wave packets; from the commutation properties of harmonic oscillator creation and annihilation operators, we find their overlap

$$\langle \quad {}_1 \,|\, {}_1 \rangle = \left\langle \left(A_y\right)_1 \middle| \left(D_x C_x J B_x\right)_1 \right\rangle^{(0)} \tag{5.29}$$

$$= iJ \quad \frac{}{2} \quad {}^4 \; area_A area_B area_C area_D e^{i(\;{}_1 \quad {}_p)t_p + i(\;{}_1 \quad {}_2 + \;{}_p)t_d}$$

$$\int_0^{{}_{vib}/2} d \;\; \exp\{i(\;{}_1 \quad {}_1) \;+\; {}^2 e^{i} \;\; (e^{i\;t_p} + e^{\;i\;t_d} \quad 1) + \;{}^2 e^{\;i} \quad 2\;{}^2\}.$$

The pulse areas, $area_I$, and dimensionless displacement, , are as defined in Appendix E.

Calculated interferograms. For chosen parameter values, Eq. (5.29) can be evaluated easily by numerical integration. We take $= 8.3 \times 10^{-4}$ a.u. $2 \;\; c(182.17\ \mathrm{cm}^{-1})$, $m = 99000\ a.u. \quad 53.917\ amu$, $d = 0.3\ a.u. \quad 0.15875$ n (${}^2 = 0.369765 \;\; = E_{FC}/$, where $E_{FC} = m \;\; {}^2 d^2/2$ is the Franck-Condon energy). Both phase-locking frequencies (see Eq. (5.21)) are chosen to match the vertical transition energy for donor excitation (${}_p = \;\; {}_d = \;\; {}_1 + E_{FC}$). Fig. 5.4 shows the calculated 2D interferogram for the case of equal site energies ${}_1 = \;\; {}_1$. The interferogram for a downhill case with ${}_1 = \;\; {}_1 \quad 2E_{FC}$ is shown in Fig. 4.5.[64]

The locations of maximal interference signal are in qualitative accord with the quasi-classical predictions of Eqs. (5.27) and (5.28) for both equal-energy and downhill cases. For the equal-energy interferogram, maxima in $\left|\langle \;\; {}_1 \,|\, {}_1 \rangle\right|$ are found when $t_p = (m + 1 \quad 0.155/2) \;\; {}_{vib}$ and $t_d = (n + 0.155/2) \;\; {}_{vib}$. Maximal signals in the downhill interferogram occur farther "off diagonal," when $t_p = (m + 1 \quad 0.5/2) \;\; {}_{vib}$ and $t_d = (n + 0.5/2) \;\; {}_{vib}$. The deviation of the effective energy transfer time ${}_{vib}/2$ from zero in the case of equal site energies can be attributed to the finite time required for the quantum

mechanical target wavepacket to leave the potential-crossing line at the Franck-Condon point.

The fringe structure in the 2D interferograms of Figs. 5.4 and 5.5 reveals amplitude-level information about the form and dynamics of the corresponding target wave packets. The rates of change with t_p and t_d of the phase $= i\ln\langle\ _1|\ _1\rangle$ are given in Eqs. (F.7) [or (F.9)] and Eqs. (F.8) [or (F.10)], respectively (see Appendix F). The last term on the right-hand side of both (F.7) and (F.8), involving the position matrix elements $\langle\ _1|q_b\ \ \bar{q}_b|\ _1\rangle$ and $\langle\ _1|q_a\ \ \bar{q}_a|\ _1\rangle$, respectively, would vanish if the reference wavepacket were the same as the target within a constant factor, as would be expected at the signal maxima in the limit of quasi-classical target-state dynamics ($E_{FC} >>$).

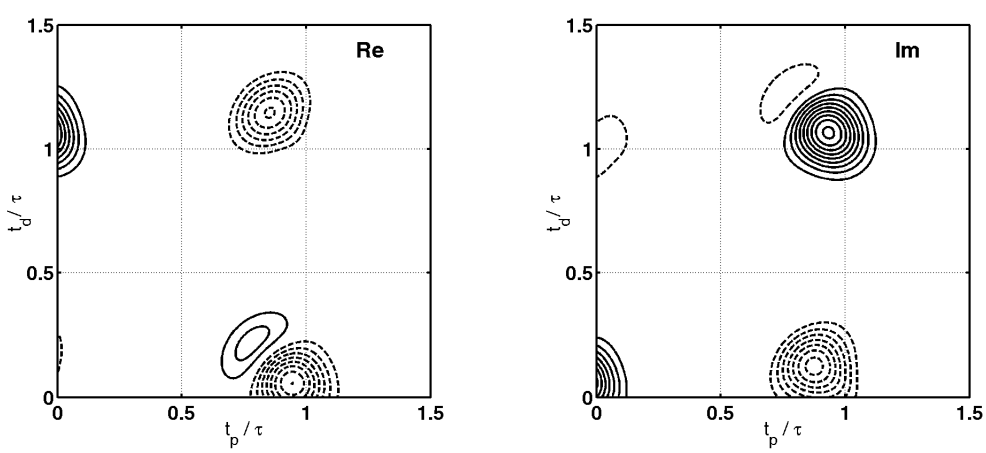

Fig. 5.4 Calculated interferogram for the case of equal site energies, $_1 = {}_{1'}$, and energy-transfer waiting time $t_w = {}_{vib}/2$. The sign and size of both the real part and the imaginary part are physically meaningful, giving the complex-valued overlap (5.29) [divided by $J(\ /2)^4\, area_A area_B area_C area_D\ _{vib}$] as a function of the intra pulse-pair delays t_p and t_d. Positive (negative) contours are given by solid (dashed) lines spaced by 0.008373, with a maximal (minimal) value +(-)0.125594.

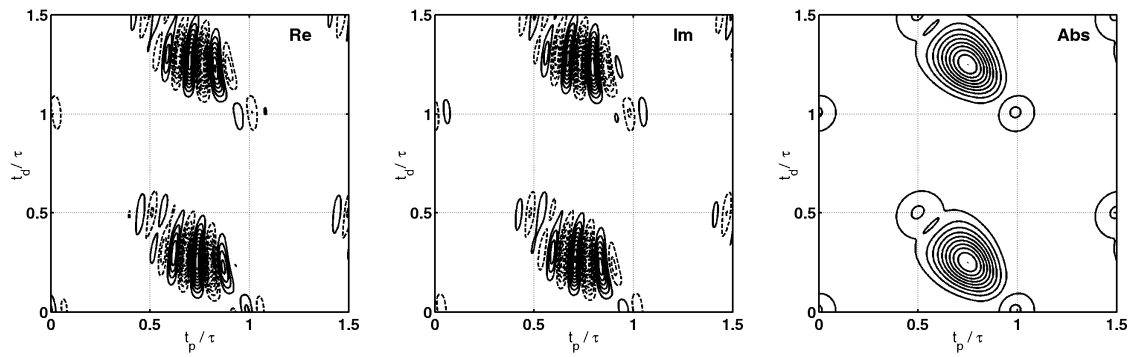

Fig. 5.5 Calculated interferogram for the case of downhill energy transfer. Same parameters as Fig. 5.4 except $_{1'} = {}_{1} \quad 2E_{FC}$. Also shown is the absolute signal intensity, in which the temporal locations of certain satellite peaks are readily discernible.

The fringe structure of the peaks in Fig. 5.4 corresponds to $/ \; t_p = \quad / \; t_d$ 0.53 at the signal maxima, and these values imply

$$\langle {}_1 | q_a \quad \bar{q}_a | {}_1 \rangle = \langle {}_1 | q_b \quad \bar{q}_b | {}_1 \rangle \quad 0.53 \frac{\langle {}_1 | {}_1 \rangle}{m \quad d} e^{i2 \quad (0.0775)}$$

for the case of equal site energies. The phase derivatives at the signal maxima in Fig. 5.5 are $/ \; t_p \quad 7.53$ and $/ \; t_d \quad 0.14$. Eqs. (F.7) and (F.8) in our case of downhill energy transfer then yield

$$\langle {}_1 | q_a \quad \bar{q}_a | {}_1 \rangle = \langle {}_1 | q_b \quad \bar{q}_b | {}_1 \rangle \quad 0.14 i \frac{\langle {}_1 | {}_1 \rangle}{m \quad d},$$

a smaller (but still non-negligible) deviation from quasiclassical behavior than in the equal-energy case.

Target and reference wave packets. In order to clarify the relationship between the experimentally measurable overlap $\langle {}_1 | {}_1 \rangle$ and the spatial form of the target and reference wave packets, we have calculated the target wavepacket using Eq. (E.5) from Appendix E and the reference with which it interferes at intra-pair delays producing maximal overlap using Eq. (E.7). These are shown in Figs. 5.6 and 5.7 for the case of equal site energies and

Figs. 5.8 and 5.9 for downhill energy transfer. The target wavepacket plotted as a function of (q_a, q_b) is seen to bear a discernible resemblance to any single peak in the corresponding interference signal plotted with respect to (t_d, t_p) (i.e. transposed about the diagonal from our Figs. 5.4 and 5.5), especially in the equal-energy case. While this vivid correspondence is a feature of the two-vibration model, it serves to illustrate that the 2D interferograms are sensitive records of the energy-transfer surface crossing *amplitude*.

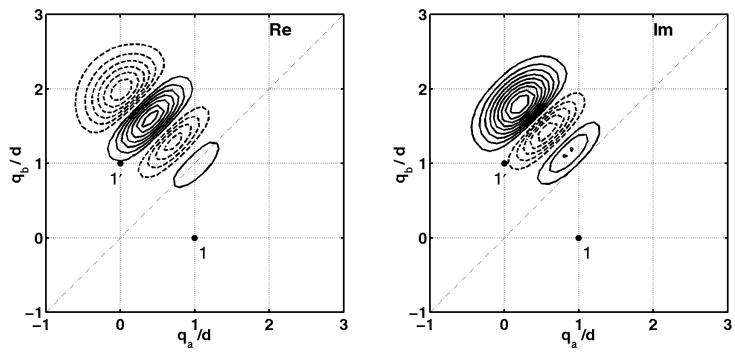

Fig. 5.6 Real and imaginary parts of the target wave packet for the equal energy case. Eq. (E.5) is plotted as $\langle q_a, q_b | \ _{1'} \rangle$ divided by $J(\ /2)area_{B\ \ vib} / d$. Contour lines of the same sign are spaced by 0.013151 and take maximal (minimal) values +(-)0.197261. Locations of potential minima for donor-excited (1) and acceptor-excited (1') states are also shown, as is the line of intersection between v_1 and $v_{1'}$.

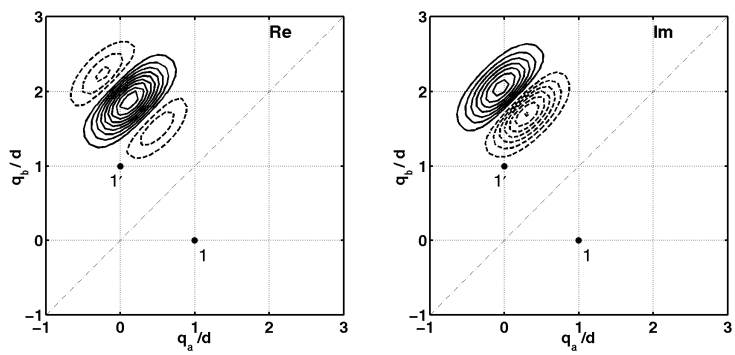

Fig. 5.7 Real and imaginary parts of the reference wave packet for the equal energy case at (t_p, t_d)$_{max}$. Eq. (E.7) is plotted as $\langle q_a, q_b | \ _{1'} \rangle$ divided by $(\ /2)^3\, area_A area_C area_D / d$. Contours of the same sign are spaced by 0.10227 and take maximal (minimal) values +(-)1.53411.

Sources for detailed features in the wavepacket interferometry signals of Figs. 5.4 and 5.5 can be identified in the corresponding target amplitudes of Figs. 6 and 8, respectively. For instance, the temporally varying signal oscillation frequency observed in Fig. 5.4 can be attributed in part to the spatially varying local de Broglie wavelengths seen in Fig. 5.6. The equal energy interferogram (Fig. 5.4) exhibits small satellite peaks near $(t_p, t_d) = (m+0.5, n+0.5)_{vib}$. Phase-space diagrams make it clear that reference wave packets prepared with these delays (not shown) will overlap the small trailing region of target amplitude near $(q_a, q_b) = (2d, 0)$ that is visible in Fig. 5.6. This trailing region of target probability amplitude arises from non-resonant electronic energy transfer late in the waiting period. The wavepacket launched by the B_x pulse reaches the outer q_a turning point on the donor-excited surface after half a period, and amplitude transfer can occur because the wavepacket lingers there for a time $\sim 2 \quad / E_{FC}$, which is only slightly longer than the local electronic nutation period $2 \quad / (v_1 \quad v_1) \sim 2 \quad / 4E_{FC}$.

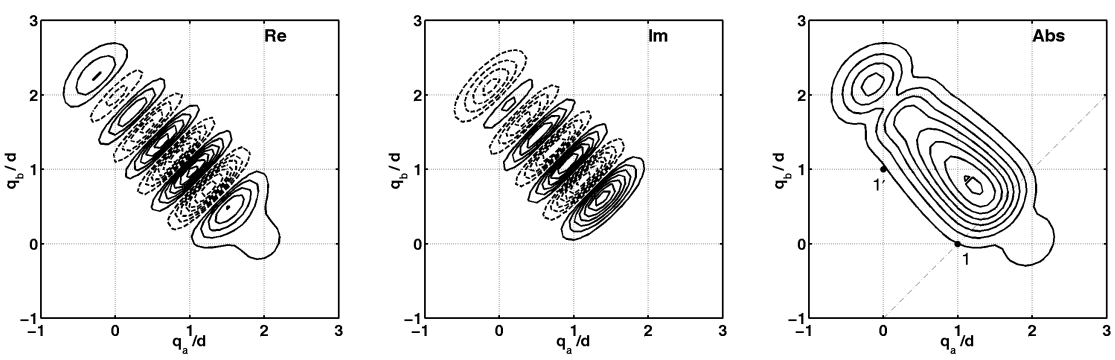

Fig. 5.8 Same as Fig. 5.6, but for the downhill case. The absolute value of the target wave packet is also plotted in order to emphasize the spatial locations of local maxima in the probability amplitude due to nonresonant electronic nutation and resonant transfer from the edges of the nuclear wave packet. Both of these secondary energy-transfer mechanisms proceed efficiently at the inner and outer turning points of motion in the donor-excited potential well.

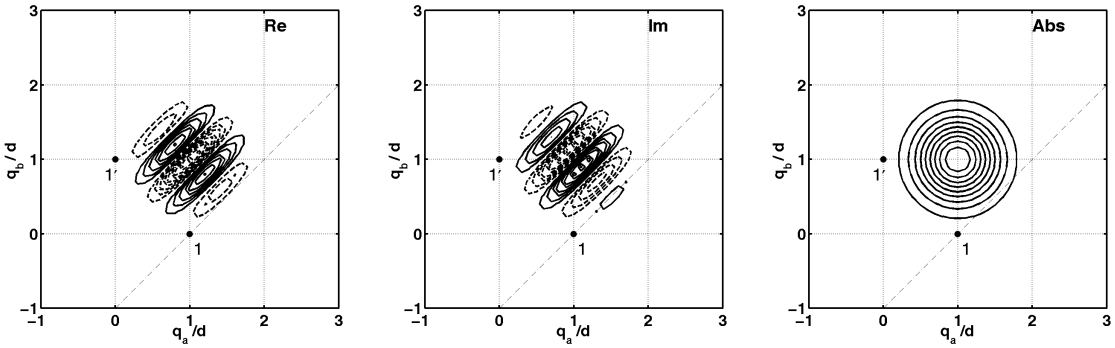

Fig. 5.9 Real part, imaginary part, and absolute value of the reference wave packet for the downhill case at $(t_p,\ t_d)_{max}$. Note the quasi-classical coherent-state structure of the reference wave packet. Plotting parameters are the same as in Fig. 5.7.

There is also a series of satellite peaks near $(t_p, t_d) = (m + 0.5, n + 0.5)\ _{vib}$ in the downhill interferogram of Fig. 5.5. These derive only in part from electronic nutation at the outer a-mode turning point (with local period $2\quad/(v_1\quad v_1) \sim 2\quad/2E_{FC}$, somewhat longer than in the equal-energy case). In the downhill case, the edge of the donor-excited wavepacket prepared by the B_x pulse still penetrates the $v_1 = v_1$ crossing region in the vicinity of $(q_a, q_b) = (3d/2, d/2)$ as the packet reaches the outer turning point, and resonant energy transfer ensues. Both of these processes contribute to the trailing region of target probability amplitude near $(q_a, q_b)\quad(2d, 0)$ in Fig. 5.8 and the corresponding satellites in the interferogram. The downhill interferogram has additional satellite peaks near $(t_p, t_d) = (m, n)\ _{vib}$. These come once again from both non-resonant electronic nutation (near $(q_a, q_b) = (0,0)$) and resonant transfer (for $(q_a, q_b)\quad(d/2,\ \ d/2)$) when the B_x wavepacket is in the Franck-Condon region. The resulting contributions to the target wavepacket evolve as a leading region of probability amplitude that is localized between $(q_a, q_b) = (0, 2d)$ and $(q_a, q_b) = (\ \ d/2, 5d/2)$ by the end of the waiting period.

Discussion

Measuring P_1 . In the case study above and Appendix D, we determined the contributions to $P_1\,(ABCD)$, that are isolable by phase cycling under various polarization combinations. While P_1 is independently observable in the sense of being the expectation value of the Hermitian operator $|1\rangle\langle 1|$ (or the quadralinear contribution to that quantity), we still need to consider how it could be measured in practice.

One strategy would be to monitor the time- and frequency-integrated *y*-polarized emission from 1 0. But any quadralinear contribution to the population of the two-exciton state 2 could give rise to *y*-polarized 2 1 emission that would obscure the sought-for signal. This complication can perhaps be overcome by the simple expedient of spectrally filtering the *y*-polarized emission. While we have assumed that $_2 = {}_1 + {}_1$ in our calculations, this is an inessential choice not strictly obeyed in practice. In actuality, the peak frequency of relaxed emission from the acceptor chromophore will depend slightly on whether the acceptor molecule is or is not electronically excited. Thus *y*-polarized emission from P_1, and P_2 should be spectrally distinguishable.

Spectral filtration of the emitted light may not be necessary in the case of downhill energy transfer, however. In this case x-*polarized* emission can serve as an independent measure of the relevant contribution to P_2 under $A_yB_xC_xD_x$. With these polarizations, the amplitudes that overlap to produce a quadralinear contribution to the population of state 2 result from the electronic transitions

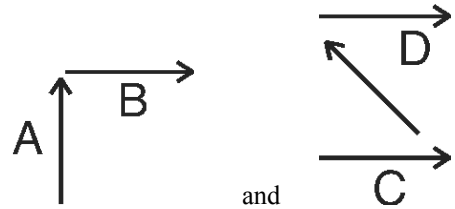

and not phase-locked (5.30)

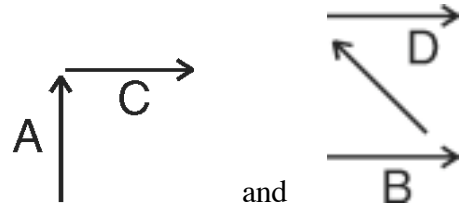

and $\exp\{-i(\ _p + \ _d)\}$ (5.31)

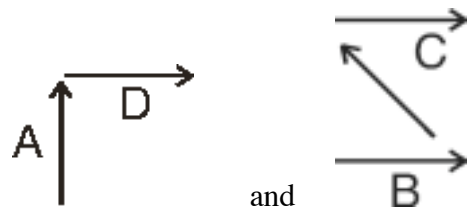

and $\exp\{-i(\ _p - \ _d)\}$ (5.32)

The phase structure of each term is indicated; there is no contribution to P_2 of zeroth order in *J*.

We showed in the case study that phase-cycling selection of the signal proportional to $\exp(\ i\ _p + i\ _d)$ could be used to extract the single overlap $\left\langle (A_y)_1 \middle| (D_x C_x J B_x)_1 \right\rangle^{(0)}$ from the other contributions to P_1. Expression (5.32) shows, though, that a portion of P_2 with the same optical phase could make an additional contribution to *y*-polarized emission. State 2 can also emit with *x*-polarization, and we can check the phase structure of the quadralinear *x*-emitting *donor* state population, $P_1(A_y B_x C_x D_x)$, to see whether an $\exp(\ i\ _p + i\ _d)$ term exists there as well. It happens that two contributions to $P_1(A_y B_x C_x D_x)$, those arising from overlaps between the amplitudes,

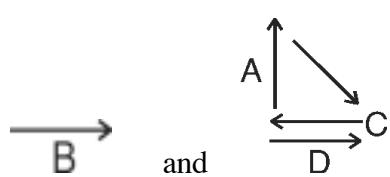

and (5.33)

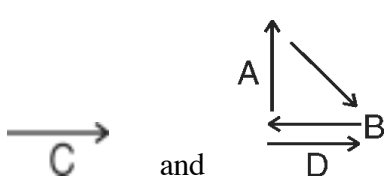

and (5.34)

both carry an $\exp(i_{p} \quad i_{d})$ phase factor; so phase-selection of the *x*-polarized emission would not generally give an unobscured view of the $\exp(\ i_{p} + i_{d})$ contribution to P_2. But the overlaps (5.33) and (5.34) involve *backward* energy transfer from the acceptor to the donor. If the acceptor site energy is sufficiently far below that of the donor (as in our downhill case, where the acceptor-excited Franck-Condon point is itself E_{FC} below the intersection energy between $v_{1'}$ and v_1), the backwards transition cannot occur for energetic reasons, and the corresponding contribution to P_1 vanishes. Thus for the downhill case, the $\exp(\ i_{p} + i_{d})$ component of P_2 can be determined as the sole contribution to *x*-polarized emission having this phase signature. Having been determined independently, this P_2 contribution can be unambiguously removed from the *y*-polarized emission without spectral filtration, leaving the sought-for overlap $\left\langle \left(A_y\right)_1 \middle| \left(D_x C_x J B_x\right)_1 \right\rangle^{(0)}$ as the only remaining signal.

Prospects for state determination. The collection of reference wave packets (5.26) available under $A_y B_x C_x D_x$ polarization is limited to both *a*-mode and *b*-mode Franck-Condon energy shells (see Fig. 5.3). The inter-pair delay $t_w = {}_{\text{vib}}/2$ places the target (5.25) on the same energy shell, allowing sizable overlap. Since reference packet formation occurs first on the v_1 surface (where only q_b is displaced) and then on v_2 (where both q_a and q_b are displaced), the prospects for determining overlaps with an exhaustive collection of reference packets—including many with average energy *off* the Franck-Condon shell—might appear dim. But measuring overlaps between target wave packets with t_w slightly different from ${}_{\text{vib}}/2$ and on-shell reference packets can be nearly equivalent to measuring overlaps between targets with $t_w = {}_{\text{vib}}/2$ and off-shell reference wave packets.

To exhibit this equivalence we note that

$$[t_w + \ t_w]_1 = [\ t_w]_0[t_w]_1 + [\ t_w]_1[t_w]_0 \tag{5.35}$$

(see footnote 53). For slight increments in waiting time, the second term in Eq. (5.35) can be neglected (unless $_1 \quad _1 \quad 4E_{FC}$, a still greater energy difference than in our downhill case), and

$$\langle\ _1 |\ _1 \rangle\Big|_{t_w + \ t_w} \tag{5.36}$$

$$= \langle n_0 | \langle 0 | A_y^\dagger[\text{-}t_p \quad t_w \quad t_w \quad t_d]_0 D_x[t_d]_0 C_x | 1 \rangle \langle 1 | [t_w + \ t_w]_1 B_x[t_p]_0 | 0 \rangle | n_0 \rangle$$

$$\langle n_0 | \langle 0 | A_y^\dagger[\text{-}t_p \quad t_w \quad t_w \quad t_d]_0 D_x[t_d]_0 C_x[\ t_w]_0 | 1 \rangle \langle 1 | [t_w]_1 B_x[t_p]_0 | 0 \rangle | n_0 \rangle$$

$$= \langle \bar{\ }_1 |\ _1 \rangle\Big|_{t_w}$$

The effective reference wavepacket $|\bar{\ }_1\rangle$ of Eq. (5.36) follows a phase-space trajectory that lies off the Franck-Condon shell for the internal vibration of the donor, increasing the dimensionality of the accessible *a*-mode phase space from one to two. This is a step toward providing an exhaustive set of reference wave packets to interfere with the target packet. To gain a second dimension in the *b*-mode space may require additional optical transitions to access state-0 or state-1 surfaces during reference state preparation.

Echo-like versus non echo-like signals. When experiments of the kind considered here are carried out on chromophores in low-temperature solids, it will be necessary to consider the effects of inhomogeneous broadening. As a result of differences in local environment, the site energies $_1$, $_1$, and $_2$ in Eqs. (5.3) through (5.6) may vary with location in the sample. This spatial inhomogeneity in the site energies could affect the nonlinear wavepacket interferometry signal from a bulk sample,[65] but in energy-transfer systems, the effects of inhomogeneity would depend on the degree of correlation between donor and acceptor energy shifts.

The simplest situation would entail perfect correlation between donor and acceptor site energies, so that $_1 = \bar{}_1 + \quad$, $_1 = \bar{}_1 + \quad$, and $_2 = \bar{}_2 + 2 \quad$. In this case, the single overlap (5.24) that is isolable under $A_y B_x C_x D_x$ polarization depends on the site-energy shift as

$$\left\langle \left(A_y\right)_1 \middle| \left(D_x C_x J B_x\right)_1 \right\rangle^{(0)} \quad \exp\{i \quad (t_p \quad t_d)\}\,, \tag{5.37}$$

and the overlap that is isolable under $A_x B_y C_x D_x$ polarization (see Eq. (A3)) goes as

$$\left\langle \left(B_y\right)_1 \middle| \left(D_x C_x J A_x\right)_1 \right\rangle^{(0)} \quad \exp\{\ i \quad (t_p + t_d)\}\,. \tag{5.38}$$

In this limiting situation, we would naturally identify the overlaps (5.37) and (5.38) as arising from echo-like and non echo-like signals, respectively; the former overlap suppresses the effects of (correlated) inhomogeneous broadening along the $t_d \quad t_p$ diagonal and the latter does not.[66]

Dynamical considerations come into play as well, however. The semiclassical criteria (5.27) and (5.28) suggest that the overlap $\left\langle \left(A_y\right)_1 \middle| \left(D_x C_x J B_x\right)_1 \right\rangle^{(0)}$ can be nonzero when the delay difference in Eq. (5.37) takes on values

$$t_p \quad t_d = (m \quad n + 1 \qquad)\ _{vib}\,, \tag{5.39}$$

some or all of which may appear off the diagonal. On the other hand, Eq. (D.7) indicates that $\left\langle \left(B_y\right)_1 \middle| \left(D_x C_x J A_x\right)_1 \right\rangle^{(0)}$ can be nonzero when

$$t_p + t_d = (n + \quad)\ _{vib}\,. \tag{5.40}$$

This time can be sufficiently short (e.g., for $n = 0$) that the non echo-like signal arising from the overlap in Eq. (5.38) would *not* be suppressed by inhomogeneous dephasing.

Related theoretical work. V. Szöcs et al.[67] very recently made a theoretical study of 2-dimensional photon echo spectroscopy on an excitonic two-site model system somewhat related to the present investigation. As a step toward a full analysis of vibrational and electronic coherence effects in photon echo signals from conjugated polymers, they considered the frequency resolved time-dependent third order polarization from a purely electronic equal-energy two-site (four-level) system. The formal treatment and specializing conditions differ in several respects from those adopted here. V. Szöcs et al. found that the positions of off-diagonal peaks in the frequency domain interferogram carry information on the energy-transfer coupling strength, the relative heights of four characteristic peaks reflect the angle between the site-localized transition dipole moments, and the peak shapes depend on the ratio of homogeneous to inhomogeneous dephasing. Consistent with the conclusions of the present study, they concluded that the (heterodyne detected) frequency domain signal carried more structural and dynamical information than its (homodyne detected) time-domain counterpart.

In an earlier and more general study, Zhang, Chernyak, and Mukamel[40] also analyzed two-dimensional electronic spectroscopy from small aggregates coupled to a vibrational bath. Like those of V. Szöcs et al.,[67] the specializing conditions of Zhang et al. are rather different from ours, and the possibility of coherent vibrational motion is suppressed. Emphasizing the structural information content of these methods, they showed how various 2D techniques could provide information on intermolecular coupling strengths and patterns. Their study did not dwell explicitly on the possibility of separately addressing donor and acceptor moieties with differently polarized pulses.[68] Interestingly, Appendix F of Ref. 40 contains expressions for the contributions to various 2D four-wave mixing signal of first order in the electronic coupling constant J.

Relationship to time-resolved CARS. Nonlinear wavepacket interferometry measurements of the kind suggested here and elsewhere[25,26] share some experimental and theoretical features with ultrafast time-resolved coherent anti-Stokes Raman scattering measurements recently made by Karavistas, Zadoyan, and Apkarian [18] The tr-CARS measurements did not involve electronic energy transfer, but—like wavepacket interferometry—are sensitive to coherently excited electronic transitions and nuclear dynamics in a low-temperature medium (I_2 in an cryogenic argon matrix), where quantum mechanical wavepacket motion is observed to play a significant role. Similar samples, along with molecular beams, could naturally be studied by wavepacket interferometry measurements as well. Consideration of time-resolved CARS from the viewpoint developed here sheds light on features of many-body coherent dynamics that will have to be taken into account in treating wavepacket interferometry data from condensed-phase samples, and highlights some differences between nonlinear wavepacket interferometry and tr-CARS.

Time-resolved CARS experiments measure the integrated intensity of a third-order signal beam, which is itself proportional to the induced electronic dipole moments $\boldsymbol{d}(t)$ (tri-linear in incident fields E_1, E_2, and E_3). The signal is given schematically by

$$S(t) \qquad dt \;\; {}^{2}_{sig}(t), \tag{5.41}$$

where

$$_{sig}(t) \qquad {}_{i} \; \ddot{\boldsymbol{d}}(t - \frac{|R - r_i|}{c}). \tag{5.42}$$

The sum in Eq. (5.42) is over chromophores in the sample volume, and the relevant portion of the dipole moment is

$$\boldsymbol{d}(t) = 2 \;\; \mathrm{Re}\left\langle n_g \middle| \langle g|[\;\; t + t_1]|g\rangle\langle e|[t \;\;\; t_3]P_3[t_3 \;\;\; t_2]P_2[t_2 \;\;\; t_1]P_1|g\rangle \middle| n_g \right\rangle, \tag{5.43}$$

where P_1, P_2, and P_3 are pulse propagators[69] that transfer amplitude between ground (g) and excited (e) electronic states, and $|n_g\rangle$ is a nuclear eigenfunction for the system as a whole (the chromophore plus the surrounding medium).[70]

In the experiments of Karavitas et al.[18] the $t_2 \quad t_1$ delay between pump and dump pulses is a small fraction of the excited state (I_2(B-state)) vibrational period. The dipole moment (5.43) can be non-zero only when $t_3 \quad t_2$ falls within one of two sequences of values (integer multiples of the vibrational period or just less than half-odd multiples of the period).[71] As observed by Karavitas and co-workers, these values of $t_3 \quad t_2$ allow the excited-state wavepacket launched by the third pulse to pass through the Franck-Condon point ($_g x, \dot{x}) = (0,0)$, giving significant overlap with the vibrational eigenfunction from which it originated (as is necessary for (5.43) to be non-zero). For $t_3 \quad t_2$ delays in the first sequence the molecule begins B-state motion while stretching (positive momentum) and for delays in the second sequence (an example of which appears in the illustration) the molecule begins B-state motion while contracting (negative momentum).

In one-dimensional wavepacket simulations of the time-resolved CARS data,[18] it was found that only the negative momentum states contributed to the signal. We can follow the explanation given for "momentum filtration" by taking account of the net effect of the small-amplitude dynamics that are induced in each of the (lower-frequency) lattice phonon modes of the Ar matrix. Because the frequency of the lattice phonon is low and its B-state displacement is small, the phonon wavepacket never gets very far from ($_{ph} q, \dot{q}) = (0,0)$ during the pulse sequence. The same is true during the short post-sequence interval $t \quad t_3$ (about equal to $t_2 \quad t_1$) needed for a negative-momentum vibration to reach ($_g x, \dot{x}) = (0,0)$. But during the longer $t \quad t_3$ (a B-state period minus $t_2 \quad t_1$) required for a positive-momentum vibration to make its way back to the Franck-Condon point, many of the lattice

modes will reach relatively large distances from $(0,0)$; the cumulative effect of the decrease in overlap in many modes will be to turn off positive-momentum contributions to the induced dipole moment (5.43).

If the $t_3 \quad t_2$ delay between the dump and re-excitation pulses becomes many times the period of the ground-state molecular vibration, then even very low-frequency lattice modes will be distributed by t_3 at many different points around their phase-space origin. Even the short $t \quad t_3$ needed for the negative-momentum molecular vibration to return to the Franck-Condon point could then produce a significant loss of overlap in the lattice degrees of freedom, contributing (along with vibrational inhomogeneity and anharmonicity) to the observed decay of the time-resolved CARS signal.

Electronic dephasing (or decoherence) effects of this kind will undoubtedly come into play in nonlinear wavepacket interferometry measurements as well. Because of the nearly-harmonic nature of low temperature host lattices, both time-resolved CARS and wavepacket interferometry experiments on chromophores in solid matrices should be valuable testing grounds for quantitative models of electronic decoherence.[72,73,74]

Concluding Remarks. Our analysis of nonlinear wavepacket interferometry for an energy-transfer complex illustrates the potential power of this form of multi-dimensional electronic spectroscopy for observing coupled electronic and nuclear dynamics of many-body condensed molecular systems at the amplitude level. Our calculations for a simple model complex show that this from of ultrafast multi-dimensional electronic spectroscopy—along with the tools of polarization spectroscopy and optical phase control—has the capacity to measure not just the evolution of electronic populations and nuclear probability densities, but the time-development of nuclear wave functions accompanying energy-transfer surface-crossing transitions.

Further research along the lines initiated here can address the important issues of multiple intra- and intermolecular modes, electronic dephasing, thermal effects, orientational disorder, and for gas phase samples, rotational dynamics and congestion. In this connection it is worth mentioning that while the treatment given in this paper is based on a pure-state description of the energy-transfer complex (in keeping with our interest in predicting and observing quantum mechanical effects), the approach is also directly applicable to isolated or condensed-phase systems with population distributed over thermally occupied levels. This generalization is accomplished formally by the elementary step of summing with Boltzmann weight over the initially populated energy states of the complex plus bath.[22] Since the numerical calculations reported here (but not the basic theoretical expressions) use laser pulses that are arbitrarily abrupt on the vibrational timescale, it will be necessary to further investigate the practical consequences of nonzero pulse duration and finite spectral bandwidth. We have specialized to pulse sequences with a few specific polarization combinations that are sensitive to the nuclear wave function arising from energy-transfer to the acceptor-excited potential energy surface. Future studies can include pulse sequences of arbitrary polarization.[75]

Notes

1. This work, originally co-authored with Prof. Jeff Cina and Dr. Dmitri Kilin, has been published in J. Chem. Phys. **118**, 46 (2003). My contributions to the work included deriving analytic expressions for the target and reference states given by Eqs, (5.25) and (5.26), deriving the signal expression given by Eq. (5.29), simulating the interferograms for equal-site and down-hill energy transfer systems shown in Figs. 5.4 and 5.5, and analyzing the wave packet dynamics using the fringe structure of the interferograms.

2. N. F. Scherer, R. Carlson, A. Matro, M. Du, A. J. Ruggiero, V. Romero-Rochin, J. A. Cina, G. R. Fleming and S. A. Rice, J. Chem. Phys. **95**, 1487 (1991).

3. N. F. Scherer, A. Matro, R. J. Carlson, M. Du, L. D. Ziegler, J. A. Cina and G. R. Fleming, J. Chem. Phys. **96**, 4180 (1992).

4. A. W. Albrecht, J. D. Hybl, S. M. Gallagher Faeder, and D. M. Jonas, J. Chem. Phys. **111**, 10934 (1999); Erratum, J. Chem. Phys. **115**, 5691 (2001).

5. W. P. de Boeij, M. S. Pshenichnikov, and D. A. Wiersma, Chem. Phys. **233**, 287 (1998).

6. L. Lepetit and M. Joffre, Opt. Lett. **21**, 564 (1996).

7. J. D. Hybl, A. Albrecht Ferro, and D. M. Jonas, J. Chem. Phys. **115**, 6606 (2001).

8. A. H. Zewail, Science **242**, 1645 (1988).

9. A. A. Mokhtari and J. Chesnoy, IEEE J. Quantum Electron. **25**, 2528 (1989); P. F. Barbara and W. Jarzeba, Adv. Photochem. **15**, 1 (1990); R. Jimenez, G. R. Fleming, P.V. Kumar, and M. Maroncelli, Nature **369**, 471 (1994); M. Chattoraj, B. A. King, G.U. Bublitz, and S. G. Boxer, Proc. Natl. Acad. Sci. USA **93**, 8362 (1996).

10. L. W. Ungar and J.A. Cina, Adv. Chem. Phys. **100**, 171 (1997).

11. See also S. Saikan, T. Nakabayashi, Y. Kanematsu, and N. Tato, Phys. Rev. B **38**, 7777 (1988); W. H. Hesselink and D. A. Wiersma, Phys. Rev. Lett. **43**, 1991 (1979).

12. M. C. Beard, G. M. Turner, and C. A. Schmuttenmaer, J. Am. Chem. Soc. **122**, 11541 (2000); O. Golonzka, M. Khalil, N. Demirdöven, and A. Tokmakoff, J. Chem. Phys. **115**, 10814 (2001); M. Zanni, N.-H. Ge, Y. S. Kim, and R. M. Hochstrasser, Proc. Natl. Acad. Sci. USA **98**, 11265 (2001).

13. L.J. Kaufman, J. Heo, L.D. Ziegler, and G.R. Fleming, Phys. Rev. Lett. **88**, 207402 (2002); K.J. Kubarych, C.J. Milne, S. Lin, V. Astinov, and R.J.D. Miller, J. Chem. Phys. **116**, 2016 (2002).

14. M. Cho, N.F. Scherer, G.R. Fleming, and S. Mukamel, J. Chem. Phys. **96**, 5618 (1992); S. Mukamel, *Principles of Nonlinear Optical Spectroscopy* (Oxford, New York, 1995).

15. Y. Tanimura and S. Mukamel, J. Chem. Phys. **99**, 9496 (1993).

16. H. Metiu and V. Engel, J. Opt. Soc. Am. B **7**, 1709 (1990). See also W.S. Warren and A. H. Zewail, J. Chem. Phys. **78**, 2279 & 2298 (1983).

17. W. Domcke and G. Stock, Adv. Chem. Phys. **100**, 1 (1997); W.T. Pollard, S. L. Dexheimer, Q. Wang, L. A. Peteanu, C.V. Shank, and R. A. Mathies, J. Phys. Chem. **96**, 6147 (1992); D. M Jonas, S. E. Bradforth, S. A. Passino, and G. R.Fleming, J. Phys. Chem. **99**, 2594 (1995); Z. Li, J. Fang, and C. C. Martens, J. Chem. Phys. **104**, 6919 (1996); C. J. Bardeen, J. Che, K.R. Wilson, V. V. Yakovlev, V. A. Apkarian, C.C. Martens, R. Zadoyan, B. Kohler, and M. Messina, J. Chem. Phys. **106**, 8486 (1997); Y.-S. Shen and J.A. Cina, J. Chem. Phys. **110**, 9793 (1999).

18. M. Karavitas, R. Zadoyan, and V. A. Apkarian, J. Chem. Phys. **114**, 4131 (2001); see also I. Pinkas, G. Knopp, and Y. Prior, J. Chem. Phys. **115**, 236 (2001).

19. E. J . Heller, J. Chem. Phys. **68**, 2066 (1978).

20. E. J. Heller, R. L. Sundberg, and D. Tannor, J. Phys. Chem. **86**, 1822 (1982); J.L. McHale, Acc. Chem. Res. **34**, 265 (2001).

21. S. Mukamel, J. Phys. Chem. **88**, 3185 (1984); Y. J. Yan and S. Mukamel, J. Chem. Phys. **88**, 5735 (1988).

22. R. A. Harris, R. A. Mathies, and W. T. Pollard, J. Chem. Phys. **85**, 3744 (1986).

23. A more general approach based on a moment expansion of physical observables, but independent of a Gaussian ansatz on the wave function or density matrix, has been recently put forward by O. V. Prezhdo and Y. V. Pereverzev, J. Chem. Phys. **113**, 6557 (2000); J. Chem. Phys. **116**, 4450 (2002).

24. See also D. J. Tannor, *Introduction to Quantum Mechanics: A Time Dependent Perspective* (University Science Books, New York, 2003).

25. J. A. Cina and R. A. Harris, J. Chem. Phys. **100**, 2531 (1994); J. A. Cina and R. A. Harris, Science **267**, 832 (1995). See also R. P. Duarte-Zamorano and V. Romero-Rochín, J. Chem. Phys. **114**, 9276 (2001); C. S. Maierle and R. A. Harris, J. Chem. Phys. **109**, 3713 (1998).

26. J. A. Cina, J. Chem. Phys. **113**, 9488 (2000).

27. T. S. Humble and J. A. Cina, Phys. Rev. Lett. **93**, 060402 (2004).

28. D. J. Tannor and S. A. Rice, J. Chem. Phys. **83**, 5013 (1985); J. Cao, J. Lumin. **87-89**, 30 (2000); R. J. Levis, G. M. Menkir, and H. Rabitz, Science **292**, 709 (2001).

29. R. Zadoyan, D. Kohen, D. A. Lidar, and V. A. Apkarian, Chem. Phys. **266**, 323 (2001).

30. R. van Grondelle, J. P. Dekker, T. Gillbro, and V. Sundstrom, Biochim. Biophys.Acta **1187**, 1 (1994); X. Hu and K. Shulten, Physics Today, August 1997, p. 28.

31. *J-Aggregates*, edited by T. Kobayashi (World Scientific, Singapore, 1996).

32. H. S. Cho, D. H. Jung, M.-C. Yoon, Y. H. Kim, Y.-R. Kim, D. Kim, S. C. Jeoung, S. K. Kim, N. Aratani, H. Shinmori, and A. Osuka, J. Phys. Chem. A **105**, 4200 (2001); C.-K. Min, T. Joo, M.-C. Yoon, C.M. Kim, Y.N. Hwang, D. Kim, N. Aratani, N. Yoshida, and A. Osuka, J. Chem. Phys. **114**, 6750 (2001).

33. F. Zhu, C. Galli, and R. M. Hochstrasser, J. Chem. Phys. **98**, 1042 (1993), Erratum, J. Chem. Phys. **98**, 9222 (1993).

34. A. Albrecht Ferro and D. M. Jonas, J. Chem. Phys. **115**, 6281 (2001)

35. Y. Sakata, T. Toyoda, T. Yamazaki, and I. Yamazaki, Tetrahedron Lett. **33**, 5077 (1992); J. A. Pescatore and I. Yamazaki, J. Phys. Chem. **100**, 13333 (1996).

36. Th. Förster in *Modern Quantum Chemistry,* part III, Edited by O. Sinanoglu (Academic Press, New York, 1965), p. 93.

37. S. Rackovsky and R. Silbey, Mol. Phys. **25**, 61 (1973).

38. T. F. Soules and C.B. Duke, Phys. Rev. B **3**, 262 (1971).

39. For a recent relaxation-theory study of vibrational effects in electronic energy transfer see M. Yang and G. R. Fleming, Chem. Phys. **275**, 355 (2002).

40. W. M. Zhang, V. Chernyak, and S. Mukamel, J. Chem. Phys. **110**, 5011 (1999). See also V. Chernyak, W. M. Zhang, and S. Mukamel, J. Chem. Phys. **109**, 9587 (1998).

41. A. J. Leggett, S. Chakravarty, A. T. Dorsey, M.P.A. Fisher, A. Garg, and W. Zwerger, Rev. Mod. Phys. **59**, 1 (1987); our reference is to a the statement on p. 15 to the effect that for practical purposes, only the population difference between the two [electronic] states was then accessible in realistic experiments.

42. In our numerical calculations, $_2$ is taken to *equal* $_1 + _1$ unless otherwise stated.

43. John Jean investigated the short-pulse-driven dynamics of a similar system in contact with a thermal reservoir in a ground-breaking study of the competition between coherence and relaxation in wave packet surface crossing: J. M. Jean, J. Phys. Chem. A **102**, 7549 (1998). See also A. Matro and J. A. Cina, J. Phys. Chem. **99**, 2568 (1995) and C. Kalyanaraman and D. G. Evans, J. Chem. Phys. **115**, 7076 (2001).

44. For plot of the adiabatic potential energy surfaces in this model, under strong and weak coupling, see Fig. 2 of Förster's article.[36]

45. In the case of equal site energies, $_1 = {}_{1'}$, the intersection between donor and acceptor surfaces includes $q_b = q_a = 0$, so energy transfer proceeds efficiently at the Franck-Condon point. When $_1 = {}_1 + m \quad {}^2 d^2 = {}_1 + 2E_{FC}$, the acceptor surface passes through the donor minimum; for continuous spectra this would be the case of maximal "Förster overlap" between donor emission and acceptor absorption. A further redshift in the acceptor absorption spectrum would lead to an inverted regime of decreasing energy-transfer efficiency.

46. The lower-case subscripts designate "preparation," "waiting," and "delay."

47. Experiments on fluorescence detection of femtosecond accumulated photon echoes have measured a similar quantity that is quadrilinear in the field amplitudes of phase-related continuous wave beams. The time resolution in those experiments was set by the field correlation time of a continuous-wave laser rather than the pulse duration. See K. Uchikawa, H. Ohsawa, T. Suga, and S. Saikan, Opt. Lett. **16**, 13 (1991); S. Saikan, K. Uchikawa, and H. Ohsawa, Opt. Lett. **16**, 10 (1991).

48. We set $\hbar = 1$ throughout this paper.

49. We specify the arbitrary initial phase so that, $[t_A \quad t_0]\| \quad (t_0)\rangle = |0\rangle|n_0\rangle$, where $|n_0\rangle$ is a vibrational eigenket of H_0 with energy E_{n_0}.

50. As defined here, the pulse propagators are anti-Hermitian: $I^\dagger = \quad I$.

51. Under these approximations, the integrand of Eq. (5.11) becomes

$$[\quad + t_I]V_I(\quad)[\quad - t_I] \qquad \frac{{}_a \; e_I}{2}\Big(|1\rangle\langle 0|e^{\;iH_1(t_I \quad)}e^{iH_0(t_I \quad)} + |2\rangle\langle 1(|e^{\;iH_2(t_I \quad)}e^{iH_{1(}(t_I \quad)}\Big)$$

$$\frac{{}_b \; e_I}{2}\Big(|1\rangle\langle 0|e^{\;iH_1(t_I \quad)}e^{iH_0(t_I \quad)} + |2\rangle\langle 1|e^{\;iH_2(t_I \quad)}e^{iH_1(t_I \quad)}\Big)\Big\}$$

$$A_I(\quad t_I)e^{\;i \quad (\quad t_I)\;i} \quad + \text{H.c.}$$

52. The expression for $|\quad {}_1\rangle$ is the same as Eq. (5.12), but with $\langle 1|$ instead of $\langle 1\,|$ on the right-hand side. The nuclear wave function in the bi-excitonic state is given by

$$|\quad {}_2\rangle = \langle 2|[t - t_D]\{D[t_d]C[t_w + t_p] + D[t_d + t_w]B[t_p] + [t_d]C[t_w]B[t_p]$$
$$+D[t_d + t_w + t_p]A + [t_d]C[t_w + t_p]A + [t_d + t_w]B[t_p]A + D[t_d]C[t_w]B[t_p]A\}|0\rangle|n_0\rangle \; .$$

53. Where $[t]_0 = \exp(\ iHt)\big|_{J=0}$ and

$$[t]_1 = \ iJ \int_0^t d\ \{|1\rangle\exp(\ iH_1(t\ \ \ ))\exp(\ iH_1\ )\langle 1| + |1\rangle\exp(\ iH_1\ )\exp(\ iH_1(t\ \ \ ))\langle 1|\}.$$

Notice that the first-order evolution operator carries a phase factor $\ \ i = e^{\ i\ /2}$ associated with the energy-transfer process, which our amplitude-sensitive measurements will be able to detect.

54. An experimental strategy for isolating the interference contribution to the population of a given electronic state with beam choppers and lock-in amplifiers was demonstrated in Refs. [2] and [3].

55. We use notation in which a bra retains the name of the ket to which it is dual: $\langle BA|$ is the bra dual to the ket $|BA\rangle$.

56. Through the pulse propagators (5.11), which involve the dot products $\ _a\ \mathbf{e}_I$ and $\ _b\ \mathbf{e}_I$.

57. P. Andrews and W.L. Barnes, Science **290**, 785 (2000).

58. In the phase-locking scheme of Scherer and co-workers,[2,3] the pulses in a phase-locked pair differ by a pure delay, and are otherwise exact copies of each other. For example, the phases-at-arrival $\ _A$ and $\ _B$ may be regarded as differing at most by an integer multiple of $2\ \ \ $. In that method, the intrapulse-pair delays (t_p) are actively stabilized and selectively undersampled so that $\ _B\ \ \ _A = 2\ N = \ _p t_p + \ _p$ for a chosen value of the locking angle $\ _p$. The same situation applies for the *CD* pulse-pair. With respect to the *inter*pulse-pair phase shifts, timing jitter on the unstabilized delay t_w allows us to regard the interpulse-pair phase shifts as random variables. For a detailed discussion of the relationship between phase shifts and time delays, see Ref. [4].

59. D. Keusters, H.-S. Tan, and W. S. Warren, J. Phys. Chem. A **103**, 10369 (1999); D. Keusters, P. Tian, W.S. Warren in OSA *Trends in Optics and Photonics, Vol. 72, The Thirteenth International Conference on Ultrafast Phenomena*, OSA Technical Digest, Postconference Edition (Optical Society of America, Washington DC, 2002), pp. 480-481.

60. A rudimentary example of phase-cycling in linear ultrafast spectroscopy can be found in Ref. [3]. There it was shown that in-phase and in-quadrature interferograms could be combined to yield the resonant part of the time-dependent linear dipole susceptibility.

61. It may be noted that while the overlaps in Eq. (5.23) depend explicitly on the observation time *t*, the isolable single overlap in Eq. (5.24) is *t*-independent. In both contributions to (5.23), one of the overlapped wavepackets evolves after t_D with a time evolution operator zeroth-order in *J* and the other with an operator linear in *J*. In the

overlap (5.24) on the other hand, both wavepackets experience evolution after t_D under the same unitary operator $[t \quad t_D]_0$ (see Eq. (5.13)); so their overlap does not change. It happens similarly, that the single overlap isolable with $A_x B_y C_x D_x$ polarization (see Appendix D) is observation-time independent. For both polarization combinations, however, it may be desirable in cases of relatively strong energy-transfer coupling to time-gate the measurement of acceptor-state population—on about a picosecond timescale—in order to ensure that the portion linear in J dominates the acceptor-state population.

62. This result has the special implication that after $(1 \quad)t_W$ of motion in the 1 -state, the a-mode target trajectory reaches a phase-point lying on the Franck-Condon energy shell; the phase-space location of the target-state a-mode will hence be accessible to a reference wavepacket after some t_d-interval of (backwards) motion in state 2. This interesting elementary feature of the transferred amplitude's motion in an energy-transfer system does not seem to have been noted previously.

63. The basic physics of this process is the same as follows the instantaneous upward displacement of the hanging point of a Hooke's-law spring holding a stationary weight: If the hanging-point is returned to its original position after $_{vib}/2$, then $(1 \quad)\ _{vib}/2$ later, the mass passes downward through the same vertical position it had at time $_{vib}/2$.

64. Equation (5.29) was integrated with a time step $_{vib}/2400$, yielding numerical errors of about a part in 10^6. The interference signals presented here supersede the preliminary calculations of D. Kilin and J. A. Cina, Ultrafast Phenomena **13**, (Springer-Verlag, 2002), conference proceedings (in press). The latter calculations were performed less accurately, by numerical diagonalization of the one-exciton subspace in the presence of a small specified value for J.

65. There does not appear to be any fundamental reason why fluorescence-detected wave packet interferometry signals could not be measured on single molecules; in which case the issue of inhomogeneous broadening would be moot if the site energies were stable for the duration of data acquisition.

66. See Chapter 10 of S. Mukamel's book, cited in Ref. [14].

67. V. Szöcs, T. Pálszegi, A. Torschanoff, and H. F. Kaufmann, J. Chem. Phys. **116**, 8218 (2002).

68. This issue is addressed, however, by O. Golonzka and A. Tokmakoff, J. Chem. Phys. **115**, 297 (2001).

69. These operators should not be confused with the similarly named interference populations of preceding paragraphs.

70. Heterodyne detection of the CARS signal — E-field interference between a signal field generated by phase-locked excitation pulses and a phase-locked local-oscillator field — would give a quantity more closely related to that measured by nonlinear wavepacket interferometry, one that is quadralinear in the external fields and linear in the third-order sample polarization.

71. Note that the phase-space diagrams considered here slightly generalize the "time circuit diagrams" of Ref. [18] by schematically indicating the intramolecular and lattice-mode dynamics that accompany the various electronic transitions.

72. J. A. Cina and R. A. Harris, Ultrafast Phenomena IX, W. Knox and P. Barbara, Eds. (Springer-Verlag, 1994) p. 486.

73. R. Silbey and R.A. Harris, J. Phys. Chem. **93**, 7062 (1989).

74. S. Jang, J. Cao, and R. J. Silbey, J. Chem. Phys. 116, 2705 (2002).

75. For instance, the uniformly polarized sequence $A_x B_x C_x D_x$ should reveal the loss of amplitude in a donor-state wavepacket of order J^2 due to electronic energy transfer. The corresponding quadralinear signal should be resistant to degradation by orientational disorder, and even provide useful amplitude-level information from a randomly oriented sample.